$CuO/ZnO/Me_xO_y/ZrO_2/SiO_2$ (Me = Mg, Ce or La) soft-templated catalysts for CO_2 hydrogenation to methanol

Luciano Atzori[1], Sarah Lai[2], Maria Giorgia Cutrufello[1,3], Francesca Ferrara[2], Alberto Pettinau[2], Mauro Mureddu[2,*], and Elisabetta Rombi[1,3,*]

[1] Department of Chemical and Geological Sciences, University of Cagliari, S.S. bivio per Sestu, 09042 Monserrato, Italy

[2] Sotacarbo S.p.A. – Grande Miniera di Serbariu, S.S. 126, 09013 Carbonia, Italy

[3] Consorzio Interuniversitario Nazionale per la Scienza e Tecnologia dei Materiali (INSTM), Via Giuseppe Giusti 9, 50121 Firenze, Italy

* Correspondence: rombi@unica.it; mauro.mureddu@sotacarbo.it

Abstract

A series of multicomponent oxide catalysts ($CuO/ZnO/Me_xO_y/ZrO_2/SiO_2$, with Me = Mg, Ce or La) was synthesized through a one-pot soft-template approach and used for CO_2 hydrogenation to methanol. In the case of the La-containing catalysts, additional samples were prepared with CuO contents in the range 40-60 wt%. The influence of the catalyst composition on the physicochemical properties as well as the effect on the catalytic performance were investigated. The fresh catalysts were characterized in terms of composition, structure, textural properties, dispersion of the oxidic phases, and reducibility. On the reduced samples, structural and acid-base properties were also investigated, as well as specific metal surface area and dispersion of Cu^0. After in situ H_2-treatment at 250 °C, the catalysts activity was tested in a bench scale plant at 250 °C and 3.0 MPa, using a gas hourly space velocity of 24000 $Ncm^3\ h^{-1}\ g_{ctz}^{-1}$ and a H_2/CO_2 molar ratio equal to 3. It was found that the production of methanol is particularly favored by the introduction of La_2O_3, the highest value of methanol space time yield (413 $mg_{CH_3OH}\ h^{-1}\ g_{cat}^{-1}$) being obtained on the $CuO/ZnO/La_2O_3/ZrO_2/SiO_2$ catalyst containing 50 wt% of copper oxide.

Keywords: Methanol synthesis; CO_2 hydrogenation; Soft-template-assisted synthesis; Promoters effect

1. Introduction

As a result of the huge amount of the greenhouse gases released into the atmosphere each year, and considering all the clear consequences for global climate, massive efforts are required to deploy technologies, policies, and business models able to quickly reduce the further release of carbon dioxide (CO_2) into the atmosphere at large scales. In this context, the share of energy produced from renewable resources, mainly solar and wind energy, has increased in recent years. Nonetheless, owing to the stochastic nature of renewable energy, suffers from supply intermittency, which current grid infrastructures cannot accommodate. In this scenario, the conversion of captured CO_2 and green hydrogen from renewable electricity into fuels such as methanol (CH_3OH) allows energy to be stored in chemical way [1]. This approach can provide a significant contribution to the decarbonization of the so-called "hard-to-abate" sectors (*e.g.*, transport and several industrial processes) by replacing the conventional fossil-derived fuels with renewable ones [2]. Based on the great significance of methanol synthesis from CO_2 hydrogenation, a new concept of "methanol economy" was originally coined by Olah [3]. Methanol is an industrial commodity used as a feedstock for several chemicals and fuels. The requirement for methanol in 2023 is expected to exceed 110 million tons and to overtake the production capacity [4]. The synthesis of methanol through CO_2 hydrogenation can be reasonably considered as a practical and feasible process to answer the question of how to replace oil and gas [3]; however, some challenges must be addressed [5] such as (i) thermodynamic limitations due to the high stability and inertness of CO_2, whose activation requires reaction temperatures higher than 240 °C, in contrast with the exothermic character of the reaction, (ii) formation of water molecules, responsible for the oxidation of Cu^0 species [6,7] and for the agglomeration of ZnO species [7], causing catalyst's deactivation, and (iii) occurrence of the reverse water gas shift reaction, which lowers selectivity towards methanol and, being endothermic, is favored at higher temperatures. To overcome these obstacles, a large variety of catalytic systems have been investigated, as demonstrated by the exhaustive reviews published in the literature [5,8-11], with the aim of developing efficient catalysts in terms of activity, methanol selectivity, and stability.

Among the heterogeneous metal-based catalysts for CO_2 hydrogenation to methanol, which principally employ Cu and noble metals such as Pd, Pt, Au, and Ag, Cu-based catalysts are considered as the most active and selective. In particular, the Cu/ZnO system is the most widely used and numerous studies have been focused on obtaining a better catalytic performance without losing the peculiar synergy between Cu and ZnO. For this purpose, different supports and/or promoters have been used such as metal oxides, including Al_2O_3, ZrO_2, Ga_2O_3, La_2O_3, CeO_2, Y_2O_3, SiO_2, TiO_2, MgO, and noble metals like Pt, Au, Rh, and Pd [8]. ZrO_2-containing catalysts demonstrated to be very active and selective in CO_2 hydrogenation due to the versatile properties and weak hydrophilic character of zirconia, which was found to enhance the Cu/Zn dispersion and the reducibility of the CuO species [12]. Suitable amount of La_2O_3 were reported to improve the production of methanol on La-Cu/ZrO_2 catalysts; a linear relationship between the conversion of CO_2 and

the Cu^0 surface area was found, whereas the selectivity to methanol was related to the distribution of basic site on the catalyst surface [13]. After introduction of both CeO_2 and La_2O_3, the performance of the Cu/Zn/Zr catalyst was found to improve due to their stronger interaction with the catalyst components that favors the H_2 spillover process [14]. CeO_2-containing catalysts were also reported to have much better catalytic performance in CO_2 hydrogenation compared with Cu/Al_2O_3, both in term of conversion and methanol selectivity, which was attributed to the exposed Cu^0 surface area and the Cu-ceria interface and surface basicity, respectively [15]. The addition of SiO_2 nanoparticles was proved to have a promotional effect on the activity of a CuO-ZnO-ZrO_2 catalytic system, which was mainly ascribed to a geometrical spacer, leading to a better inter-dispersion of metal oxides components and then to an increase of Cu^0 surface area as well as surface basicity of the resulting CuO-ZnO-ZrO_2-SiO_2 catalysts [16]. Cu^0 dispersion and metallic surface area were also found to highly increase after MgO addition to Cu/ZnO/ZrO_2 [17] and Cu/γ-Al_2O_3 catalysts [18].

Along with the catalyst composition, the synthesis method also has a deep influence on the final performance of the catalyst. Apart from conventional coprecipitation, the most adopted preparation procedure, other methods have also been developed [8], including combustion synthesis [19], precipitation-reduction route [20,21], sol-gel synthesis [22], deposition-precipitation [23], citrate decomposition [24], reverse coprecipitation [25], and impregnation [26].

Due to the high specific surface area, pore structure and wide pore size, mesoporous metal oxides have been considered as promising candidates for the catalytic conversion of CO_2 [27]. For the synthesis of these mesoporous solids, the soft-template co-precipitation method has proved to be highly efficient by virtue of its ability to tune the morphology and the physico-chemical properties of the final catalysts [28]. Numerous works can be found in the literature dealing with the soft template synthesis of mixed oxides as catalysts for different applications such as CO oxidation [29], photodecomposition of wastewater [30], and photocatalytic degradation of azo dyes [31] and rhodamine [32]. However, only a few works deal with the synthesis of Cu-based catalysts for CO_2 hydrogenation to methanol through the soft-template approach, among them the interesting studies by Li et al. [33] and Marcos et al. [34], where Cu-ZnO-ZrO_2 catalysts were prepared by a surfactant-assisted co-precipitation method.

Taking into consideration the efficiency of the soft-template method compared to conventional synthesis procedures in obtaining high surface area mesoporous materials, in this work, a series of multicomponent oxide catalysts (CuO/ZnO/Me_xO_y/ZrO_2/SiO_2, with Me = Mg, Ce or La) were synthesized via the one-pot soft-template method and tested in the hydrogenation reaction of CO_2 into methanol at 250 °C, 3.0 MPa, and gas hourly space velocity (*GHSV*) of 24000 $Ncm^3\ h^{-1}\ g_{ctz}^{-1}$. The catalysts were deeply characterized with different techniques as for the composition, structural and textural properties, reducibility, and surface basic properties with the aim of investigating the effect of different promoters on their physico-chemical features and the catalytic performance. On the La-promoted catalysts, the influence of the Cu content was also studied on samples with CuO loadings in the range 40-60 wt%.

2. Materials and experimental details

2.1. Catalysts preparation

2.1.1. Materials

All chemicals were of analytical grade and used as received without further purification. Hexadecyltrimethylammonium bromide (CTAB, ≥98%), sodium carbonate (Na_2CO_3, 99%), sodium hydroxide (NaOH pellets, 98%), nitric acid (HNO_3, 69 %), copper (II) nitrate hydrate ($Cu(NO_3)_2{\cdot}2.5H_2O$, 98%), aluminium nitrate nonahydrate ($Al(NO_3)_3{\cdot}9H_2O$, ≥98%), zinc nitrate hexahydrate ($Zn(NO_3)_2{\cdot}6H_2O$, 98%), zirconium (IV) oxynitrate hydrate ($ZrO(NO_3)_2{\cdot}6H_2O$, 99%), magnesium nitrate hexahydrate (Mg(NO3)2·6H2O, 99%), cerium (III) nitrate hexahydrate ($Ce(NO_3)_3{\cdot}6H_2O$, 99%), lanthanium nitrate ($La(NO_3)_3{\cdot}6H_2O$, 99.9%), were purchased by Sigma-Aldrich (St. Louis, Missouri, USA). Silica (SiO_2 Aerosil 200) was supplied by Degussa. Lithium tetraborate ($Li_2B_4O_7$, 99,998%) was provided by Alfa Aesar.

2.1.2. Synthesis of catalysts

A series of mesoporous *x*CuO/*y*ZnO/zMeO/*v*ZrO_2/*w*SiO_2 multicomponent oxide catalysts (with Me = Mg, Ce or La) were synthesized with different compositions, using the Soft-Template (ST) method [35,36]. For a typical synthesis, an appropriate amount of the template was dissolved at room temperature in 100 cm^3 of distilled water under stirring, to which a certain amount of the nitrate precursors was added (CTAB/nitrate precursors = 0.62 mol mol^{-1}). The sol was stirred for 30 min, after that a 0.17 mol L^{-1} solution of NaOH was added dropwise until a pH value of 13 was reached and maintained under stirring for 15 h. After digestion at 90 °C for 3 h, the precipitate was separated by filtration and washed with hot distilled water (70 °C). The solid was dried at 110 °C for 6 h and finally calcined at 450 °C for 3 h. The obtained materials are labelled as CuZnMeZrSi(*x*/*y*/z/*v*/*w*), where Me = Mg, Ce, La and the numbers in brackets denote the nominal weight percentages of the different oxides.

2.2. Catalysts characterization

The chemical composition of the soft-template-derived mixed oxides was determined by inductively coupled plasma optical emission spectroscopy (ICP-OES) with a 5110 ICP-OES spectrometer (Agilent Technologies). Samples (*ca.* 0.05 g) were calcined at 500 °C for 12 h, mixed with lithium tetraborate (1:15 w/w), placed in a platinum crucible, and then fused at 1000 °C in a furnace for 30 min. After cooling of the melt, the resultant fusion bead was dissolved at 80 °C for about 30 min with 20 mL of a HNO_3 solution (0.80 M) and finally diluted to the desired volume by Milli-Q water.

The X-ray diffraction (XRD) analysis was performed both on the as-prepared and H_2-treated (5 vol% H_2 in N_2; flow rate, 15 cm^3 min^{-1} at 250 °C for 2 h) samples. XRD patterns were recorded on a X'pert Pro diffractometer (Panalytical, Malvern, UK) with a θ-θ Bragg-Brentano geometry, a Cu-Kα wavelength radiation (λ = 1.5418 Å), and a X'Celerator

detector operating at 40 kV and 40 mA. The crystallite size was estimated by the Scherrer equation using the Warren correction [37].

Textural analysis was carried out with an ASAP 2020 apparatus (Micromeritics, Norcross, Georgia, USA) by determining the nitrogen adsorption/desorption isotherms at −196 °C. Prior to the analysis, the samples were pre-treated overnight under vacuum (10^{-3} Pa) at 250 °C for 12 h. The Brunauer-Emmett-Teller (BET) specific surface area and the specific pore volume were assessed from the adsorption data [38].

Temperature-programmed reduction (TPR) profiles were recorded on a TPD/R/O 1100 apparatus (Thermo Fisher Scientific, Waltham, Massachusetts, MA, USA) under the following conditions: sample weight, 0.030 g; heating rate (from 40 to 400 °C), 10 °C min^{-1}; flow rate, 30 cm^3 min^{-1}; H_2 concentration, 5 vol% in N_2. Prior to the experiment, samples were pretreated in nitrogen (20 cm^3 min^{-1}) at 350 °C for 2 h. The hydrogen consumption was monitored by a thermal conductivity detector (TCD).

The copper dispersion and the specific metal surface area were evaluated by N_2O adsorptive decomposition at controlled temperature (N_2O reacts with metallic Cu on the catalyst surface to form Cu_2O and N_2), followed by H_2 temperature-programmed-reduction of the Cu_2O surface layers formed [39]. Analyses were performed on the TPD/R/O instrument mentioned above using the following procedure: *ca.* 0.1 g of fresh catalyst was first exposed to a H_2/N_2 mixture (H_2, 5 vol% in N_2; flow rate, 15 cm^3 min^{-1}) at 250 °C for 2 h for reducing copper oxide to metallic copper; then, pulses of N_2O (0.347 cm^3) were admitted to the sample at 40 °C using He as the gas carrier (100 cm^3 min^{-1}). The oxidation of the surface metallic copper to Cu(I) was considered complete when the area of the N_2O pulses remained constant, indicating that the reactant was no longer consumed in the reaction. Finally, a H_2-TPR run (H_2, 5 vol% in N_2; flow rate, 20 cm^3 min^{-1}) was performed from 40 to 400 °C (heating rate, 10 °C min^{-1}). The copper dispersion (D_{Cu^0}) and the Cu specific metal surface area per mass of catalyst (A_{Cu^0}) were calculated by the following equations:

$$D_{Cu^0} = \frac{n_{H_2} \cdot \alpha_{Cu/H_2} \cdot M_{Cu}}{W_{Cu}} \cdot 100$$

$$A_{Cu^0} = \frac{n_{H_2} \cdot \alpha_{Cu/H_2} \cdot N_A}{\rho_{Cu^0}} \cdot 100$$

where n_{H_2} are the moles of H_2 consumed per mass of catalyst, α_{Cu/H_2} is the stoichiometric ratio (2 mol_{Cu} $mol_{H_2}^{-1}$), M_{Cu} is the copper molar mass, W_{Cu} is the bulk copper content (weight fraction), N_A is the Avogadro constant ($6.022 \cdot 10^{23}$ atoms mol^{-1}), and ρ_{Cu^0} is the copper surface density ($1.46 \cdot 10^{19}$ atoms m^{-2}). Calibration of the H_2 amount consumed was previously carried out by using a copper oxide standard.

Adsorption microcalorimetry measurements were performed with a Tian-Calvet heat flow calorimeter (Setaram, Caluire, France), equipped with a volumetric vacuum line. Each sample (*ca.* 0.1 g, 40-80 mesh), as prepared or previously H_2-treated (5 vol% H_2 in N_2; flow rate, 15 cm^3 min^{-1}) at 250 °C for 2 h, was thermally pretreated at 220 °C for 12 h under vacuum ($5 \cdot 10^{-3}$ Pa). Adsorption was carried out by admitting successive doses of the probe gas (NH_3 or CO_2) at 80 °C in order to limit physisorption. The equilibrium pressure relative to each adsorbed amount was measured by means of a differential pressure gauge and the thermal effect was recorded. The run was stopped at a final equilibrium pressure of 133 Pa.

Transmission electron microscopy (TEM) and Energy Dispersive X-Ray (EDX) analyses were performed on a JEOL JEM 1400-PLUS microscope (JEOL, Akishima, Tokyo, Japan) equipped with an energy dispersive X-ray system and operating at an accelerating voltage of 120 kV. Finely ground powders of the samples were first dispersed in ethanol and sonicated. The resulting suspensions were dropped onto 200 mesh carbon-coated copper grids.

2.3. Catalytic tests

The performance evaluation for CO_2 hydrogenation to methanol was investigated in a customized Microactivity Efficient, PID Eng&Tech bench-scale plant, employing a high-pressure fixed bed stainless steel reactor (9.1 mm I.D. x 304.8 mm long). A porous plate (made of Hastelloy C, 20 μm in size) and a quartz wool were used to support the catalytic bed inside the reactor. For the reaction tests, the reactor was loaded with 0.5 g of catalyst previously diluted with 3 g of α-Al_2O_3, in order to obtain a total bed volume equal to 3 cm^3 (isothermal temperature zone of the reactor). Prior to catalytic testing, the fresh catalyst was reduced in-situ in a stream of 15% v/v H_2/N_2 at 250 °C for 2 h under atmospheric pressure. Upon completion of the reduction process, the system was maintained at 250 °C, and the reaction gas mixture containing H_2 and CO_2 (molar ratio 3:1) and 10 vol% of N_2 (used as internal standard for gas-chromatographic analysis) was fed. The CO_2 hydrogenation reaction was then carried out at 3.0 MPa and at Gas Hourly Space Velocity (*GHSV*) of 24000 Ncm^3 g_{cat}^{-1} h^{-1} (or 4000 h^{-1}, if referred to the whole bed volume).

The reaction stream was analyzed by a gas chromatograph (Agilent 7890B) equipped with two different columns linked in series. In particular, a HP-Plot Q column (30 m · 0.53 mm · 40 μm) was used to separate CO_2, methanol, dimethyl ether and C_2 - C_3 species, while a HP-PLOT Molesieve 5A (30 m · 0.53 mm · 50 μm) column was employed to separate H_2, N_2, CH_4 and CO. The columns were connected to a conductivity detector (TCD), used for the quantification of permanent gases, and a flame ionized detector (FID) for the analysis of the carbon-containing compounds. To avoid condensation of condensable products, connections between plant gas outlet and GC inlet were heated at 180 °C. The steady state activity measurements were taken after 1 h on stream and the reaction was performed for 24 h.

The results of the quantitative analysis of the carbon-containing components were used for checking the carbon mass balance and for calculating CO_2 conversion (X_{CO_2}) and products selectivity (S_i) values through the following equations, where $\dot{n}_i$ are the molar flow rates:

$$X_{CO_2} = \frac{\left(\frac{\dot{n}_{CO_2}}{\dot{n}_{N_2}}\right)_{in} - \left(\frac{\dot{n}_{CO_2}}{\dot{n}_{N_2}}\right)_{out}}{\left(\frac{\dot{n}_{CO_2}}{\dot{n}_{N_2}}\right)_{in}} \cdot 100 \qquad S_i = \frac{\left(\frac{\dot{n}_i}{\dot{n}_{N_2}}\right)_{out}}{\left(\frac{\dot{n}_{CO_2}}{\dot{n}_{N_2}}\right)_{in} - \left(\frac{\dot{n}_{CO_2}}{\dot{n}_{N_2}}\right)_{out}} \cdot 100$$

The space time yield of methanol (STY_{CH_3OH}), *i.e.*, the amounts of methanol produced per gram of catalyst *per* hour ($mg_{CH_3OH}\ g_{cat}^{-1}\ h^{-1}$), was determined by the formula:

$$STY_{CH_3OH} = \frac{\frac{Y_{CH_3OH}}{100} \cdot \left(\dot{n}_{CO_2}\right)_{in} \cdot MW}{m_{cat}} \cdot 1000$$

where Y_{CH_3OH} is the yield of methanol, $(\dot{n}_{CO_2})_{in}$ is the inlet CO_2 molar flow rate, MW is the molecular weight of methanol, and m_{cat} is the catalyst weight.

The catalytic tests were repeated three times on selected samples, with a relative error always lower than 2 % estimated for the values of conversion, selectivity, and yield.

3. Results and discussion

3.1. Characterization of fresh samples

The chemical composition of the as-prepared CuZnMeZrSi(v/w/x/y/z) catalysts is reported in Table 1, where their textural features are also summarized.

The N_2 physisorption isotherms of all the samples (Figure 1) show the presence of a narrow hysteresis loop, which is related to a mesoporous character mainly ascribable to the aggregation of particles of different size and shape [38]. All the samples with a CuO content equal to 40 wt% are characterized by S_{BET} values higher than 130 $m^2\ g^{-1}$ (Table 1), which confirm the ability of the soft-template method to obtain materials with a high specific surface area. At variance with the introduction of CeO_2 and La_2O_3 promoters, which do not affect the S_{BET} with respect to that of the unpromoted CuZnZrSi(40/20/30/10) catalyst, the addition of MgO seems to be efficient in promoting the development of a higher surface area. In the case of the La-containing catalysts, the increase in CuO content results in a remarkable decrease in S_{BET}, in particular when passing from 40 wt% to 50 wt%. This trend could be related to the concomitant decrease in both

the SiO_2 and ZrO_2 amounts for the CuZnLaZrSi(50/19/5/21/5) and CuZnLaZrSi(58/22/5/10/5) samples [12,16]. It appears from TEM images in Figure 2 that CuZnZrSi(40/20/30/10) and CuZnLaZrSi(40/15/5/30/10) are made up of small, rounded nanoparticles; at increasing CuO content, they seem to partly organize into chains forming rod-like particles, whose aggregation reduces mesoporosity and surface area.

Table 1. Chemical composition of the prepared oxide catalysts.

Sample	Composition[(a)]					Textural properties[(b)]	
	CuO (wt%)	**ZnO** (wt%)	**M_xO_y** (wt%)	**ZrO_2** (wt%)	**SiO_2** (wt%)	**S_{BET}** ($m^2\ g^{-1}$)	**V_p** ($cm^3\ g^{-1}$)
CuZnZrSi(40/20/30/10)	39.7	22.6	-	31.7	6.0	132	0.19
CuZnMgZrSi(40/15/5/30/10)	39.4	16.8	5.4	32.1	6.3	164	0.26
CuZnCeZrSi(40/15/5/30/10)	38.9	17.9	5.0	31.9	6.3	135	0.16
CuZnLaZrSi(40/15/5/30/10)	39.0	17.6	5.1	32.3	6.0	132	0.18
CuZnLaZrSi(50/19/5/21/5)	50.5	19.6	4.8	21.0	4.2	76	0.19
CuZnLaZrSi(58/22/5/10/5)	58.3	23.4	4.7	10.4	3.1	65	0.24

[(a)] Determined by ICP-OES analyses. [(b)] Determined through N_2 physisorption measurements.

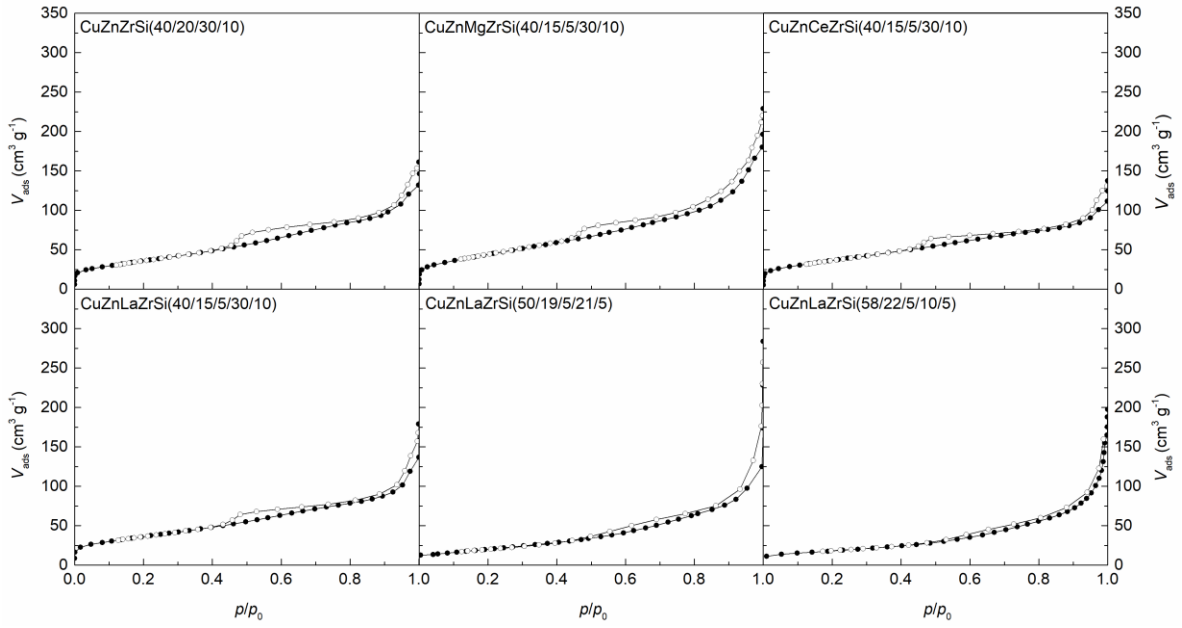

Figure 1. N_2 physisorption isotherms of the fresh samples.

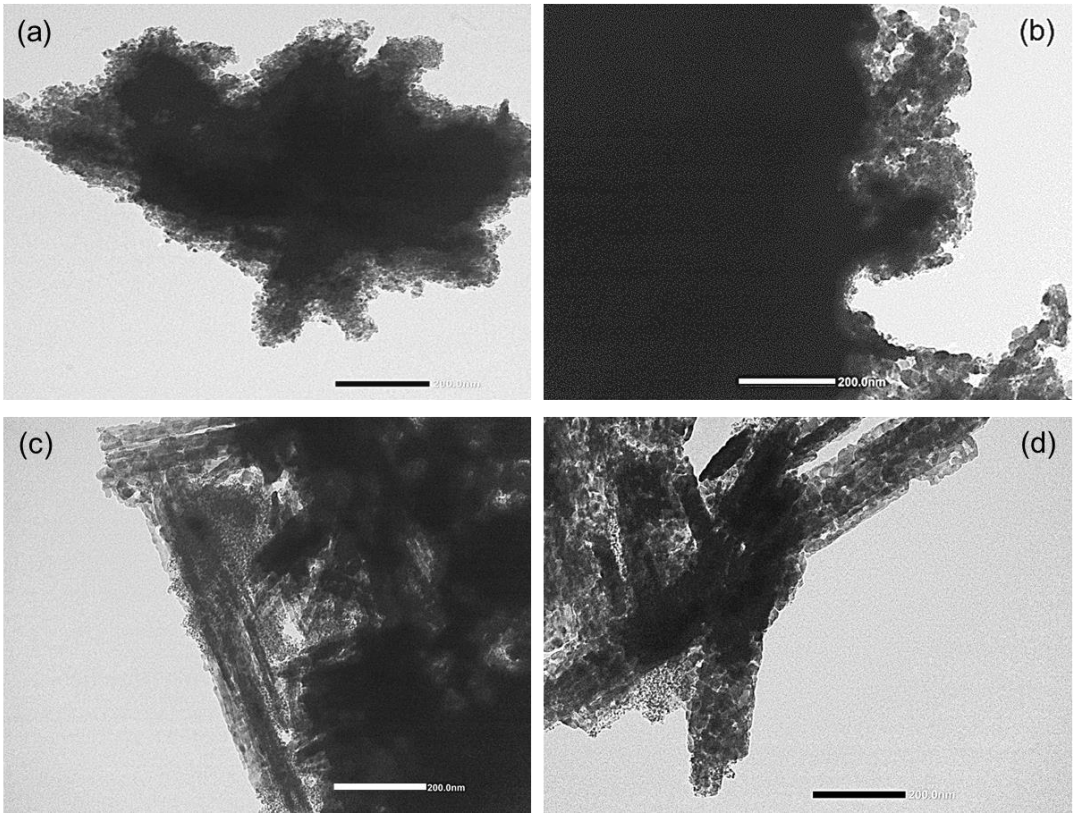

Figure 2. TEM images of CuZnZrSi(40/20/30/10) (a), CuZnLaZrSi(40/15/5/30/10) (b), CuZnLaZrSi(50/19/5/21/5) (c), and CuZnLaZrSi(58/22/5/10/5).

The X-ray diffraction patterns are shown in Figure 3. All the samples exhibit the typical reflections of the monoclinic CuO phase (PDF Card 045-0937), whose intensities are found to increase along with the copper content. The size of CuO crystallites, calculated by the Scherrer equation in the range 7-14 nm, can only be considered as a rough estimate, because of the superimposition of the most intense peaks of tenorite to wider signals. For the catalysts with a CuO content of 40 wt%, no clear peaks ascribable to crystalline phases of ZnO, ZrO_2, SiO_2, and oxidic promoters (MgO, CeO_2, or La_2O_3) are detected, suggesting their presence in amorphous or highly dispersed forms. On the other hand, very small signals related to the hexagonal ZnO phase (zincite, PDF Card 036-1451) are observable for CuZnLaZrSi(50/19/5/21/5) and CuZnLaZrSi(58/22/5/10/5), for which both the CuO and ZnO amounts are increased. Although, as expected, the intensity of these peaks increases along with the ZnO content, their presence on the CuZnLaZrSi(50/19/5/21/5) sample, for which the amount of ZnO (19.6 wt%) is only slightly higher than that of CuZnLaZrSi(40/15/5/30/10) (17.6 wt%), seems to suggest that rather than to the higher ZnO content they are due to a worsening of the zincite dispersion. This hypothesis seems to be supported by the absence of zincite reflections in the XRD pattern of the unpromoted CuZnZrSi(40/20/30/10) catalyst despite having a ZnO content of 22.6 wt%. The trend of ZnO dispersion with the increase in the CuO loading

could be explained by the concomitant decrease in the amounts of ZrO_2 and SiO_2, which instead favor its dispersion [12,16].

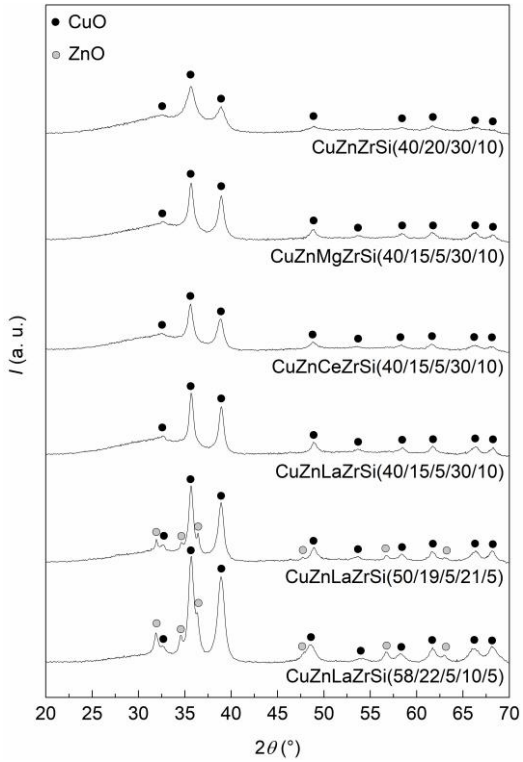

Figure 3. XRD patterns of the fresh samples.

To study the reducibility of the soft-templated samples, H_2 temperature programmed reduction (H_2-TPR) analyses were performed, and the results are presented in Figure 4. For each sample, only one contribution is observed in the range 150-340 °C. Since ZnO [40], La_2O_3 [41], MgO [42], ZrO_2 [43], and SiO_2 [44] are not reducible in the temperature range adopted for the TPR analyses, the observed contribution can exclusively be ascribed to the reduction of CuO species. However, in the case of the CuZnCeZrSi(40/15/5/30/10), a minor contribution ascribable to the surface reduction process of ceria at temperatures higher than 300 °C cannot be ruled out [45]. Interestingly, the position of the maximum in the TPR profile results to be shifted to higher temperature (from 264 to 287 °C) in presence of the promoters, indicating the occurrence of stronger CuO-Me_xO_y interactions, which make the copper oxide species more difficult to reduce. A more accurate inspection of the TPR profiles reveals that they result from the overlapping of different contributions: the appearance of a tail towards the lower temperatures seems to indicate the existence of highly dispersed CuO clusters (α-species), while the more or less defined shoulder in the main contribution, ascribable to β-species [34,46] suggests the presence of CuO made up of nanoparticles of different sizes, being the smaller particles more easily reducible than the larger ones [47]. The reduction extent for the samples, calculated by determining the amount of H_2 consumed in the

reduction process from the area under the TPR curve and considering a Cu^{2+}:H_2 stoichiometry of 1:1, was found to be ≥ 95%.

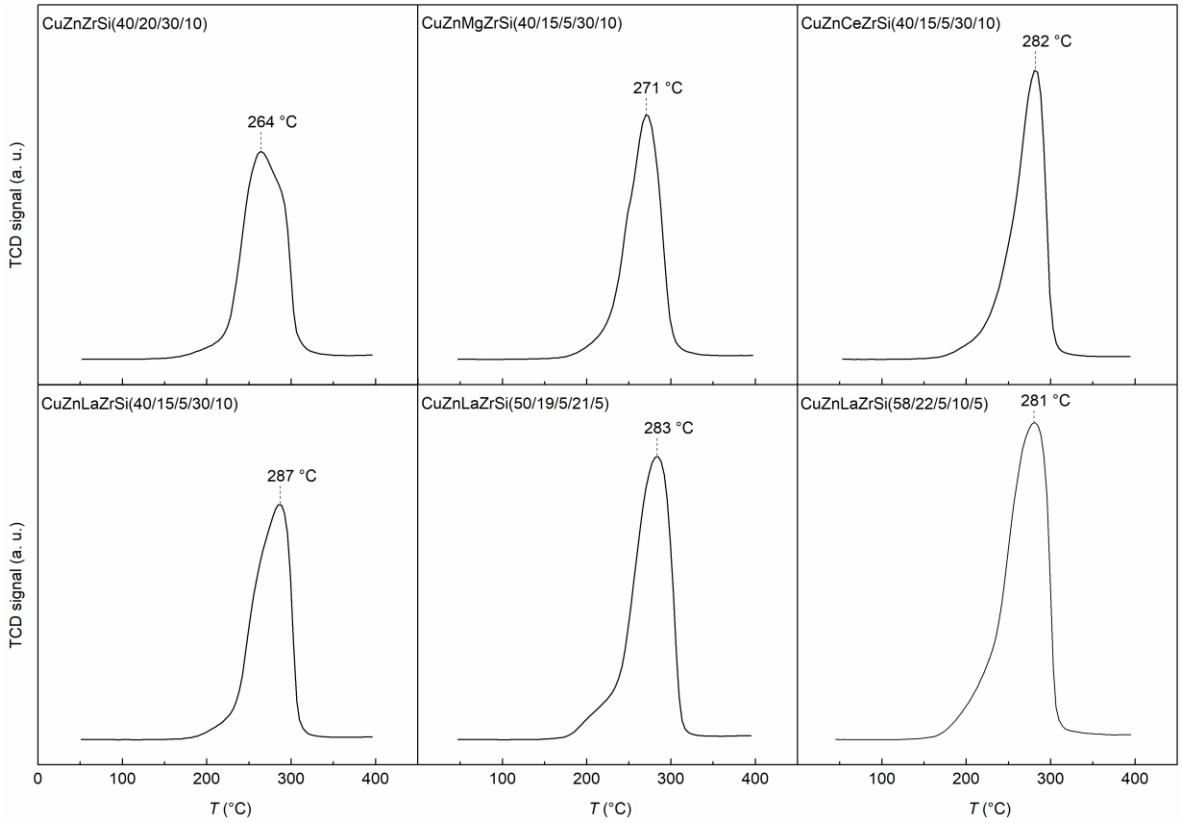

Figure 4. H_2-TPR profiles of the as-prepared samples.

3.2. Characterization of H_2-treated samples

XRD patterns of the catalysts after H_2-treatment at 250 °C are shown in Figure 5. As expected, for all the reduced samples, signals of metallic copper (PDF Card 04-0836) are present, from which an average crystallites size in the range 15-19 nm was roughly estimated. Compared to the fresh samples, no differences are observed in the reflections ascribable to zinc oxide, which appear clearer due to the disappearance of the copper oxide signals.

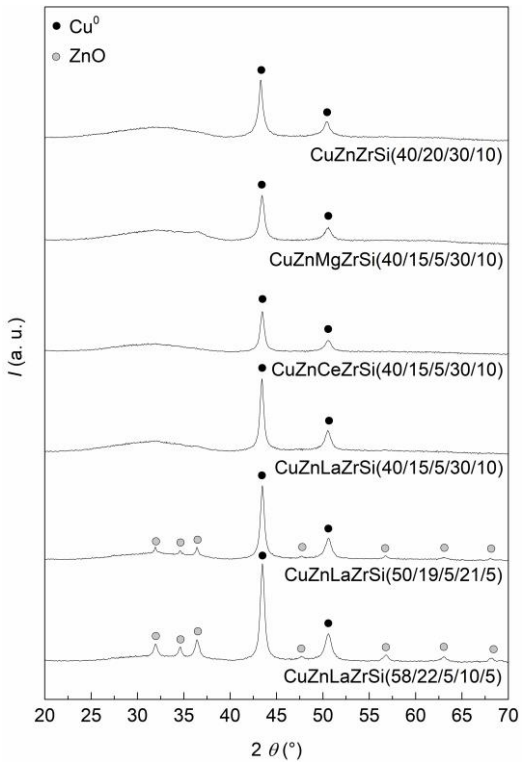

Figure 5. XRD patterns of the reduced catalysts.

The specific metal surface area of Cu^0 was determined by means of the N_2O dissociative adsorption analyses. The calculated values, expressed per catalyst mass unit (A_{Cu}), are reported in Table 2 together with the copper dispersion (D_{Cu}). All samples exhibit high values of both Cu^0 surface area and dispersion, which appear considerably higher than those reported in the literature for Cu-ZnO-ZrO_2 catalysts synthesized through the surfactant-assisted co-precipitation technique [33,34]. Compared to the unpromoted CuZnZrSi(40/20/30/10) catalyst, it emerges that A_{Cu} is positively affected by the addition of the oxide promoters, except for the CeO_2-containing sample, which shows the lowest value of such parameter. Among all the promoters, MgO results particularly beneficial, leading to an increase in the A_{Cu} value of *ca.* 24% (from 11.7 to 15.5 $m^2\ g^{-1}$) with respect to the unpromoted sample. Noteworthy, for the La_2O_3-containing catalysts, the metal surface area increases with the copper content and the Cu^0 dispersion does not vary significantly, despite the remarkable decrease in S_{BET}.

Table 2. Specific metal surface area and copper dispersion for the H_2-treated catalysts.

Sample	Cu (wt%)	D_{Cu}[(a)] (%)	A_{Cu}[(a)] ($m^2\ g_{cat}^{-1}$)
CuZnZrSi(40/20/30/10)	31.7	5.7	11.7
CuZnMgZrSi(40/15/5/30/10)	31.5	7.6	15.5
CuZnCeZrSi(40/15/5/30/10)	31.1	4.0	8.2
CuZnLaZrSi(40/15/5/30/10)	31.1	6.4	12.9
CuZnLaZrSi(50/19/5/21/5)	40.3	5.9	15.5
CuZnLaZrSi(58/22/5/10/5)	46.6	6.6	19.8

(a) Calculated from N_2O dissociative adsorption measurements.

Adsorption microcalorimetry of NH_3 and CO_2 was used in order to investigate the acid and base properties, respectively. The results are shown in Figures 6 and 7 and summarized in Table 3. For all the samples, trends of the differential adsorption heat (Q_{diff}, kJ mol^{-1}) are reported as a function of the amount of the adsorbing sites (n, μmol g^{-1}) to obtain information on the influence of the surface coverage on the energetics of the adsorption. The cut-off value between chemisorption and physisorption (the latter corresponding to Q_{diff} as low as 2-3 times the condensation heat of the probe molecule [48]) was fixed at 60 kJ mol^{-1} for the acid sites (n_A) and 40 kJ mol^{-1} for the basic ones (n_B), being the heat of condensation at 80 °C equal to 20.2 and 13.7 kJ mol^{-1} for NH_3 and CO_2, respectively [48]; thus, sites with lower adsorption heats have been disregarded in evaluating the acid-base properties of the surface. The strength distribution of the sites was assessed by roughly ranking them as strong ($n_{A,s}$, $n_{B,s}$: $Q_{diff} \geq 150$ kJ mol^{-1}), medium-strength ($n_{A,m}$, $n_{B,m}$: $100 \leq Q_{diff} < 150$ kJ mol^{-1}), and weak ($n_{A,w}$: $60 \leq Q_{diff} < 100$ kJ mol^{-1}; $n_{B,w}$: $40 \leq Q_{diff} < 100$ kJ mol^{-1}) (Table 3).

For all the catalysts, a steep decrease in Q_{diff} (whose initial values are in the range 370-250 kJ mol^{-1}) below 150 kJ mol^{-1} is observed at low NH_3 uptakes (< 25 μmol g^{-1}), which indicates that strong acid sites are present in low amounts (Figure 6). The continuous decreasing trend of the Q_{diff} *vs.* ammonia uptake profiles in the region of chemical adsorption is indicative of a heterogenous surface from the energetic point of view. From Figure 6a and Table 3, it emerges that, compared to the CuZnZrSi(40/20/30/10) sample, the acid properties seem to be little affected by the nature of the promoter oxide in the CuZnMeZrSi(40/15/5/30/10) series. On the other hand, for the CuZnLaZrSi catalysts, it can be observed (Figure 6b) that the curves for the catalysts with higher CuO contents tendentially lie below the curve of the sample containing 40 wt% of CuO and reach the cut-off value (60 kJ mol^{-1}) at notably lower ammonia coverages, which clearly indicates a decrease in the acid surface properties at increasing amounts of copper oxide. This is due to the reduction in the amount of weak and medium-strength acid sites with the increase in the CuO content from 40 up to 58 wt% (Table 3).

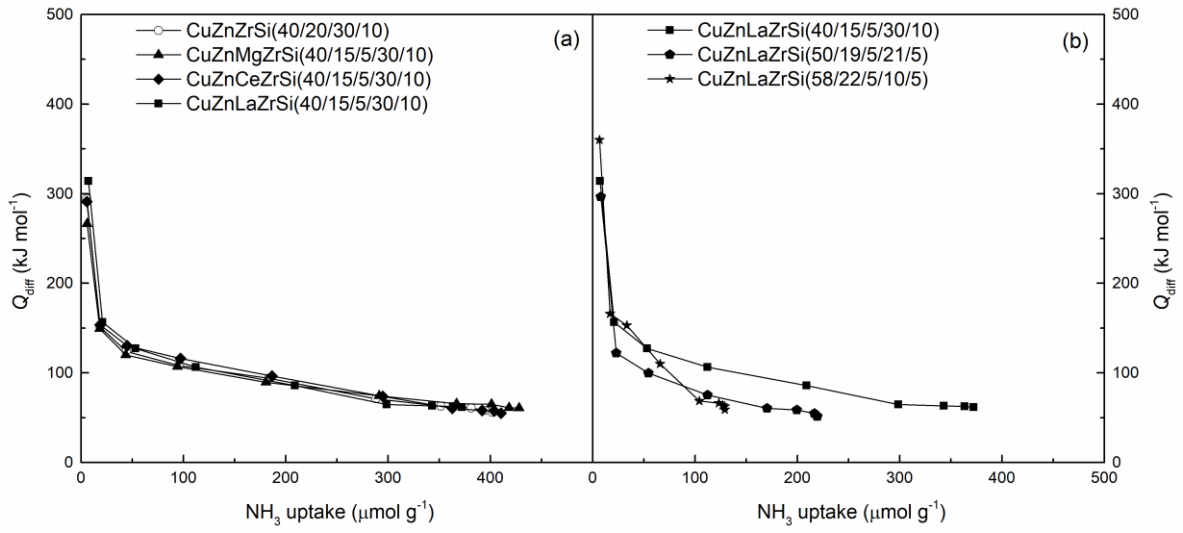

Figure 6. Differential heat of adsorption (Q_{diff}) as a function of ammonia coverage for the H_2-treated catalysts in the presence of: (a), different Me_xO_y (Me = Mg, Ce, La) oxides as promoters (5 wt%); (b), different CuO loadings for La_2O_3 promoted samples.

Concerning basicity, the curves of Q_{diff} as a function of the CO_2 adsorbed amount show, for all the catalysts, a continuously decreasing trend that reaches the characteristic values of non-specific adsorption (40 kJ mol^{-1}) at low coverages (< 15 μmol g^{-1}) (Figure 7). The initial values of Q_{diff} are in the range 215-100 kJ mol^{-1}, pointing out that not all catalysts have strong basic sites. At variance with the case of acidity, the basic character of CuZnZrSi(40/20/30/10), which does not possess strong sites, appears to increase by adding 5 wt% of MgO or CeO_2, while unexpectedly the addition of La_2O_3 does not introduce strong basicity and decreases at the same time the number of weak and medium strength sites (Table 3). The increase in the amount of CuO from 40 to 50 wt% results in a remarkable increase in basicity for the CuZnLaZrSi(50/19/5/21/5) sample (Figure 7b), particularly in the number of the strong and weak sites (Table 3). On the other hand, the further increase in the CuO content to 58 wt% determines a notable worsening of the basic surface properties (Figure 7b). This trend could be explained by considering that Cu^0 crystallites formed as a result of the reduction process may have covered the surface to a greater extent, limiting the accessibility to the basic sites.

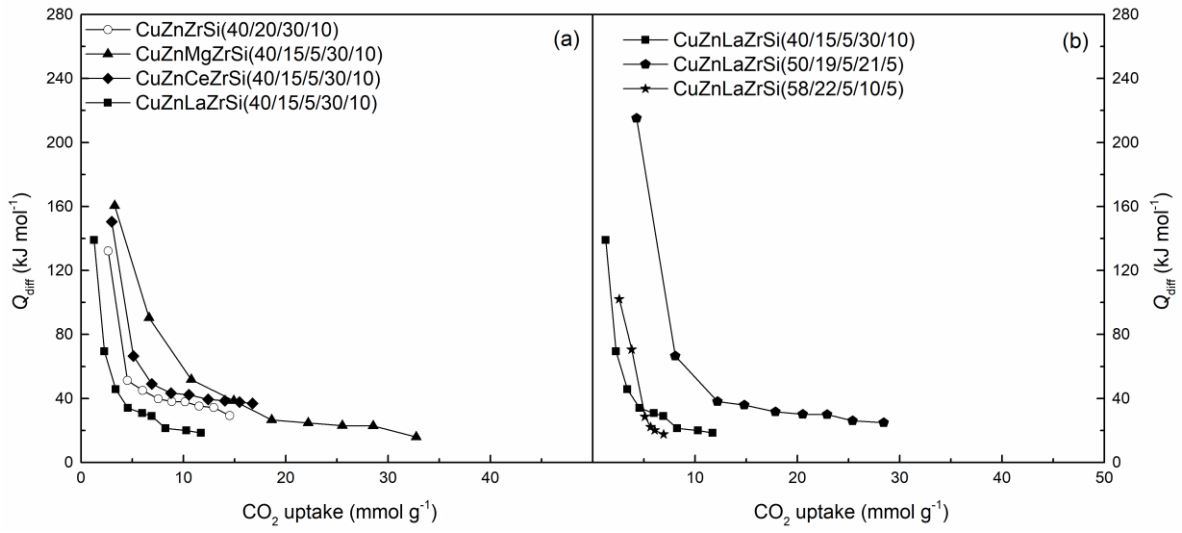

Figure 7. Differential heat of adsorption (Q_{diff}) as a function of carbon dioxide coverage for the H_2-treated catalysts in the presence of: (a), different Me_xO_y (Me = Mg, Ce, La) oxides as promoters (5 wt%); (b), different CuO loadings for La_2O_3 promoted samples.

Table 3. Acid and basic sites strength distribution for the H_2-treated catalysts.

Sample	n_A (μmol g^{-1})				n_B (μmol g^{-1})			
	$n_{A,w}$[(a)]	$n_{A,m}$[(b)]	$n_{A,s}$[(c)]	$n_{A,tot}$[(d)]	$n_{B,w}$[(e)]	$n_{B,m}$[(f)]	$n_{B,s}$[(g)]	$n_{B,tot}$[(h)]
CuZnZrSi(40/20/30/10)	241	125	20	386	4	3	0	7
CuZnMgZrSi(40/15/5/30/10)	298	112	18	428	8	2	4	14
CuZnCeZrSi(40/15/5/30/10)	200	148	23	371	8	1	3	12
CuZnLaZrSi(40/15/5/30/10)	228	116	28	372	2	2	0	4
CuZnLaZrSi(50/19/5/21/5)	125	34	21	180	5	1	6	12
CuZnLaZrSi(58/22/5/10/5)	53	40	36	129	2	3	0	5

Acid sites (n_B): [(a)] $60 \leq Q_{diff} < 100$ kJ mol^{-1}; [(b)] $100 \leq Q_{diff} < 150$ kJ mol^{-1}; [(c)] $Q_{diff} \geq 150$ kJ mol^{-1}; [(d)] $Q_{diff} \geq 60$ kJ mol^{-1}. Basic sites (n_A) [(e)] $40 \leq Q_{diff} < 100$ kJ mol^{-1}; [(f)] $100 \leq Q_{diff} < 150$ kJ mol^{-1}; [(g)] $Q_{diff} \geq 150$ kJ mol^{-1}; [(h)] $Q_{diff} \geq 40$ kJ mol^{-1}.

3.3. Catalytic results

On the *in-situ* reduced samples with H_2 at 250 °C, the reaction tests were performed at 250 °C, 3.0 MPa, and *GHSV* = 24000 $Ncm^3 h^{-1} g_{cat}^{-1}$. After reaching the steady state in the first hour, the catalysts were found to be stable within the investigated time on stream (Figure S1). Under the conditions of the catalytic tests, the main carbon-containing products were methanol and carbon monoxide, formed through the CO_2 hydrogenation and the reverse water-gas shift reactions, respectively (Scheme 1). Dimethyl ether (DME), ethane (C_2), and propane (C_3) were detected in very low amounts, while methane was not observed. The catalytic results, expressed in terms of CO_2 conversion (X_{CO_2}), selectivity

to the products (S_i), and methanol yield (Y_{CH_3OH}) and space time yield (STY_{CH_3OH}), are summarized in Table 4 as average values determined over 24 h of reaction.

$$CO_2 + 3H_2 \rightleftarrows CH_4 + 2H_2O \qquad \Delta H^0 = -49.5 \text{ kJ mol}^{-1} \qquad (1)$$

$$CO_2 + H_2 \rightleftarrows CO + H_2O \qquad \Delta H^0 = +41.2 \text{ kJ mol}^{-1} \qquad (2)$$

Scheme 1. Stoichiometric equations for: (1) CO_2 hydrogenation to methanol; (2) reverse water-gas shift reaction.

Table 4. Catalytic results (average values over 24 h on stream) for CO_2 hydrogenation to methanol. Reaction conditions: T = 250 °C; P = 3.0 MPa; H_2/CO_2 = 3 mol mol^{-1}; $GHSV$ = 24000 Ncm^3 g$_{cat}^{-1}$ h^{-1}.

Sample	X_{CO_2} (mol%)	S_{CO} (mol%)	S_{CH_3OH} (mol%)	$S_{(DME+C_2+C_3)}$ (mol%)	Y_{CH_3OH} (mol%)	STY_{CH_3OH} (mg_{CH_3OH} g_{cat}^{-1} h^{-1})
CuZnZrSi(40/20/30/10)	9.0	51.8	48.0	0.2	4.32	344
CuZnMgZrSi(40/15/5/30/10)	8.9	52.9	47.0	0.1	4.18	318
CuZnCeZrSi(40/15/5/30/10)	6.9	42.4	57.4	0.2	3.96	303
CuZnLaZrSi(40/15/5/30/10)	9.8	51.9	47.9	0.2	4.69	357
CuZnLaZrSi(50/19/5/21/5)	10.1	46.6	53.3	0.1	5.38	413
CuZnLaZrSi(58/22/5/10/5)	12.7	62.5	37.4	0.1	4.75	363

It can be observed that the catalytic performance depends on the nature of the promoter. By comparing the CuZnMeZrSi catalysts with a CuO loading of 40 wt%, it appears that the Mg- and Ce-promoted catalysts show a lower STY_{CH_3OH} (Table 4), due to a lower methanol selectivity and to a considerable decrease in CO_2 conversion in the case of Cu/Zn/Mg/Zr/Si and Cu/Zn/Ce/Zr/Si, respectively. This result could be explained by the lower ZnO content of the Me-promoted catalysts (Table 1), according to similar outcomes described in other papers [49-51], in which was reported that the reduction of the zinc oxide content into the catalyst formulation generally leads to a worsening of the catalytic performance. However, it is worthy of note that, despite the lower ZnO content, the La-containing sample performs better than the unpromoted CuZnZrSi(40/20/30/10) catalyst, showing a higher CO_2 conversion with the same selectivity to methanol and thus achieving the highest value of methanol productivity (357 mg_{CH_3OH} g_{cat}^{-1} h^{-1}). This result suggests that the ZnO content is not the unique parameter that affect the catalytic performance.

A significant decrease in CO_2 conversion in the presence of ceria was already observed for CuZnAl mixed oxides prepared from hydrotalcite-type precursors [52], Cu-ZnO systems supported on $Zr_xCe_{(1-x)}O_2$ ($0 \leq x \leq 1$) [53], and $CuZnMO_x$ systems (M = Al, Zr, Ce, Ce-Zr) [54], which was ascribed to its lower efficiency in improving the textural

properties and metal surface area of the catalysts. Such effect seems to be confirmed also in the present work, being the Cu/Zn/Ce/Zr/Si(40/15/30/5/10) sample characterized by the lowest value of Cu^0 metal surface area (Table 2).

Noteworthy, a general increasing trend (Figure 8) is found for X_{CO_2} as a function of the specific Cu^0 surface area (A_{Cu}), with the exception of the CuZnMgZrSi sample, which shows a CO_2 conversion unexpectedly low by considering its high A_{Cu} value (Table 2). This fact was already observed by other authors [55], who reported that a decrease in CO_2 conversion is observed when an excess of MgO is added to a Cu/ZrO_2-based catalyst, despite its ability in favoring a high Cu^0 specific surface area. According to what reported in the literature [56], such behavior could be explained by taking into account the basic properties of MgO, on whose surface sites very stable carbonate species can be formed, thus hindering CO_2 conversion.

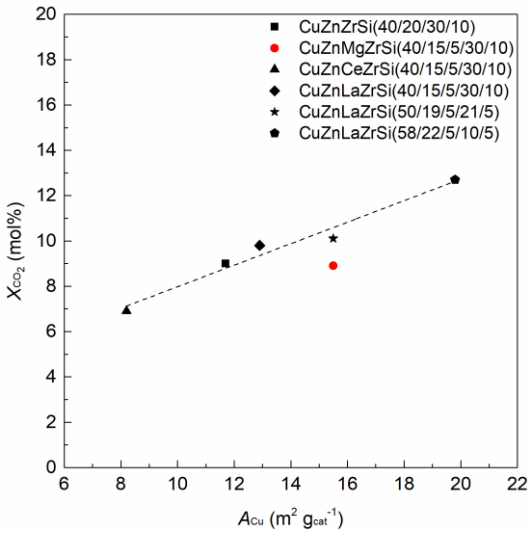

Figure 8. CO_2 conversion (X_{CO_2}) as function of Cu^0 specific surface area (A_{Cu}) for all the prepared CuZnMeZrSi(v/w/x/y/z) catalysts.

The positive effect of the presence of La_2O_3 on the CO_2 conversion could instead be ascribed to its ability in promoting both strong CuO-La_2O_3 interactions, as highlighted by the TPR results (Figure 3), and high Cu^0 dispersion and specific surface area (Table 2). To confirm the ability of lanthana to favor the homogeneous dispersion of the CuO phase, Energy Dispersive X-Ray (EDX) chemical mapping and linear profile analyses were performed on the unpromoted (Figure S2) and La-promoted (Figures S3-S5) catalysts. As can be seen from Figure S2a, the chemical mapping highlights a homogeneous dispersion of the atomic species Zn, Zr, and Si, while Cu appears not uniformly distributed, as also shown by the linear profile analysis (Figure S2b). By converse, for the La-containing catalysts, both the chemical mapping (Figures S3a-S5a) and the linear profile analyses (Figures S3b-S5b) indicate a very good dispersion of Cu regardless of

its amount; the other components also appear to be well distributed throughout the particle, with the exception of Zn, which seems to be a little segregated in the case of the CuZnLaZrSi(58/22/5/10/5) catalyst.

Concerning methanol selectivity, it is found that it tendentially increases as the CO_2 conversion decreases (Figure 9), with the Ce-promoted catalyst showing the highest S_{CH_3OH} value (57.5 mol%). Such a general behaviour seems to suggest that CO could be produced not only through the RWGS mechanism (Scheme 1) but also by the possible secondary reaction of methanol decomposition into CO and H_2:

$$CH_3OH \rightleftarrows CO + 2H_2 \qquad \Delta H^0 = -90.6 \text{ kJ mol}^{-1} \qquad (3)$$

This hypothesis is supported by what reported by other authors [57], who observed that the contribution of this reaction becomes more significant at increasing conversions.

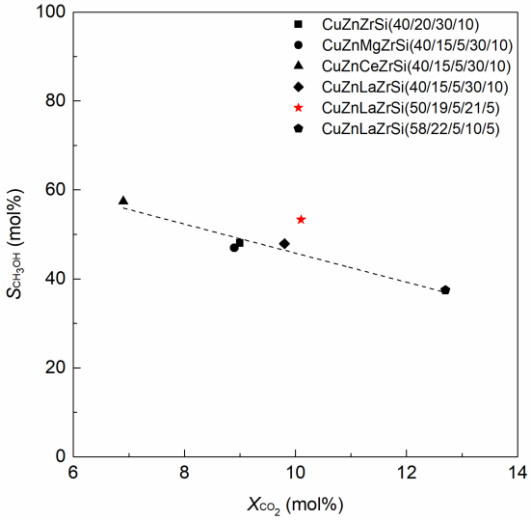

Figure 9. Methanol selectivity (S_{CH_3OH}) as a function of CO_2 conversion (X_{CO_2}) for all the prepared CuZnMeZrSi(v/w/x/y/z) catalysts.

Considering the promising catalytic performance obtained with the CuZnLaZrSi(40/15/30/10) sample, the effect of different CuO contents was studied on additional La-promoted catalysts. It is found that CO_2 conversion increases with the copper oxide content (Table 4) and also with the specific Cu^0 surface area (Figure 8). Concerning methanol selectivity, it can be noted that the CuZnLaZrSi(50/19/5/21/5) catalyst does not follow the general trend of S_{CH3OH} as a function of X_{CO2} (Figure 9), showing a surprisingly high methanol selectivity (53.3 mol%). As a consequence, it exhibits the highest value of methanol space time yield (413 mg_{CH_3OH} g_{cat}^{-1} h^{-1}), as shown in Figure 10, where STY_{CH_3OH} is reported as a function of the copper loading. According to the results reported by Gao and co-authors on the performance of

Cu/Zn/Al/Zr catalysts [58], whereas the number of exposed Cu^0 sites affects CO_2 conversion, methanol selectivity seems to depend more on the number of the surface basic sites. Indeed, CO_2 adsorption microcalorimetry pointed out that CuZnLaZrSi(50/19/5/21/5) has the highest basicity among the La-containing catalysts (Table 3). This could be explained by the considerable enrichment of La on the surface (6.25 wt% compared to 4.10 wt% in the bulk), as revealed by EDX analysis (Table S1). The higher amount of exposed La_2O_3 can reasonably be considered as responsible for the higher basicity of this catalyst and consequently for its better catalytic performance in terms of S_{CH_3OH} and STY_{CH_3OH}.

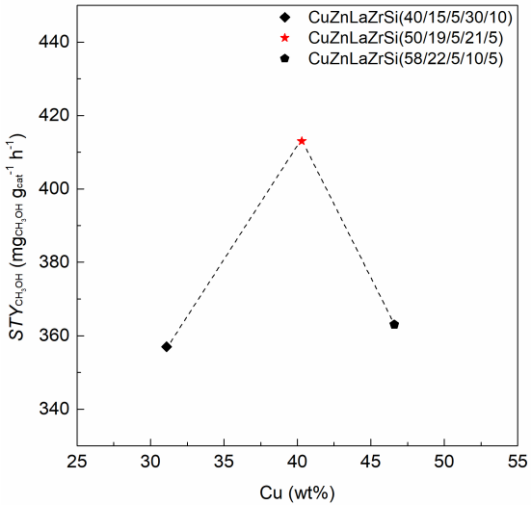

Figure 10. Methanol space time yield (STY_{CH_3OH}) as a function of Cu content.

In agreement with other authors [59,60], the obtained results indicate that the Cu^0 surface area cannot be considered as the only crucial parameter for obtaining high catalytic activity. Indeed, not a simple correlation probably exists between single properties of the Cu/ZnO-based samples and their catalytic performance, which could be simultaneously dependent on different parameters, related both to the nature of the promoters and the catalyst composition. Indeed, it should be considered that a modification of the relative amount of the oxidic components inevitably occurs as a consequence of the introduction of the promoters and/or the change of the CuO content. The observed trend of STY_{CH_3OH} as a function of copper content, which shows a maximum (Figure 10) despite the continuous increase in A_{Cu} with the same parameter, further supports the view that the catalytic activity does not depend only on the specific metal surface area. The decay of the catalytic performance passing from 50 wt% to 58 wt% of copper could be explained by the worsening of the ZnO dispersion, as indicated by XRD results, and by the significant decrease in S_{BET} value (Table 1), which can probably be due to the excessive diminution of the ZrO_2 and SiO_2 percentages (Table 1). Therefore, it seems to appear that optimization of the relative amounts of all components is necessary to maximize the synergistic effect in the catalytic

process. However, to confirm this aspect, further investigation is needed to systematically explore a wider range of relative concentrations of the different components.

The results obtained on the present Cu/Zn/La/Zr/Si(50/19/5/21/5) catalyst, which showed the best catalytic performance, are compared in Table 5 with recent literature data, relating to systems as similar as possible in terms of nature of the used chemical constituents and obtained under comparable operating conditions. When expressed as $g_{CH_3OH}\ mL^{-1}\ h^{-1}$, the calculated value of the methanol space yield for the CuZnLaZrSi(50/19/5/21/5) catalyst (0.069 $g_{CH_3OH}\ mL^{-1}\ h^{-1}$) is lower than those reported in the literature by Gao et al. [61,62] and by Dong et al. [63] for Cu/Zn/Al/Zr [61], CuZnAl [62], and Cu/Zn/Zr [63] systems. However, it must be considered that the reactions were performed in more severe conditions than ours in terms of pressure (5 MPa). On the other hand, at comparable operating conditions (250 °C and 3 MPa), the CuZnLaZrSi(50/19/5/21/5) catalyst exhibits the highest methanol productivity (0.413 $g_{CH_3OH}\ g_{cat}^{-1}\ h^{-1}$) in comparison with the other catalytic systems [50,64-68], which show values in the range 0.05-0.376 $g_{CH_3OH}\ g_{cat}^{-1}\ h^{-1}$. Moreover, it is worthy of note that all the CuZnMeZrSi catalysts studied in this work also show good catalytic performances in terms of methanol productivity, with STY_{CH_3OH} values varying between 0.318 and 0.363 $g_{CH_3OH}\ g_{cat}^{-1}\ h^{-1}$.

Table 5. Comparison of the catalytic data obtained for the most promising CuZnLaZrSi(50/19/5/21/5) catalyst with the significant catalysts reported in the recent literature.

Catalyst	X_{CO_2} (mol%)	STY_{CH_3OH} ($g_{CH_3OH}\ g_{cat}^{-1}\ h^{-1}$)	(*T* - *P*) (°C - MPa)	*GHSV* (h^{-1})	**Reference**
Cu/Zn/Al//Zr	17.3	0.12 ($g_{CH_3OH}\ mL^{-1}\ h^{-1}$)	250 - 5.0	4000	[61]
Cu/Zn/Al	20.2	0.11 ($g_{CH_3OH}\ mL^{-1}\ h^{-1}$)	250 - 5.0	4000	[62]
$Cu/ZnO/ZrO_2$	15.4	0.16 ($g_{CH_3OH}\ mL^{-1}\ h^{-1}$)	230 - 5.0	4600	[63]
Cu/Zn/Zr	ca. 8.5	0.126	250 - 3.0	24000 (mL $g_{cat}^{-1}\ h^{-1}$) [(a)]	[64]
$La_{0.8}Cu_{0.7}Zn_{0.3}O_x$	6.4	0.05	250 - 5.0	3600	[65]
$CuO\text{-}ZnO/Al_2O_3$	5	0.10	250 - 3.0	3600	[66]
$CuO\text{-}ZnO/SiO_2$	1	0.06	250 - 3.0	3600	[66]
Cu/Zn/Zr/Mg/Al	ca. 11.4	0.066	250 - 2.0	3000	[67]
Cu/Zn/Ga	10.3	0.109	250 - 3.0	3000	[68]
$Cu/ZnO/ZrO_2$-SBA-15	19.2	0.376	250 - 3.0	6600	[50]
CuZnLaZrSi(50/19/5/21/5)	10.1	0.413	250 - 3.0	4000	[This work]

[(a)] same value as that used in this work.

4. Conclusions

Different oxide CuZnMeZrSi catalysts (with Me = Mg, Ce or La) were synthesized through a one-pot soft-template method and used for the methanol synthesis by CO_2 hydrogenation. Additional La-containing catalysts were also prepared by varying the copper oxide content in the range 40-60 wt%. XRD patterns of the fresh samples with a CuO amount of 40 wt% showed only the reflections of the tenorite phase, suggesting that all the other components are present in a highly dispersed and/or amorphous form. For the La-containing samples with higher CuO loading, peaks ascribable to the zincite phase were also observed, indicating the worsening of the ZnO dispersion. Compared to CuZnZrSi, the presence of the metal oxide promoter decreased the reducibility of the CuO species as a result of increased Cu-Me interactions. Except for CeO_2, all the promoters were found to favor Cu^0 dispersion and metal surface area, especially in the case of MgO, while the acid-base properties were only slightly affected irrespective of the nature of the oxide. A general increasing trend was observed for CO_2 conversion *vs.* Cu^0 specific surface area, while methanol selectivity was found to tendentially decrease with the increase in conversion, probably due to the occurrence of the methanol decomposition reaction.

However, it emerged that, beside the Cu^0 specific surface area, different parameters, which depend on both the nature and the relative concentration of the catalyst components, simultaneously affect the catalytic performance. This fact is confirmed by the low conversion of the Mg-containing catalyst in relation to its high Cu^0 dispersion, and by the high methanol selectivity of the CuZnLaZrSi(50/19/5/21/5) sample in relation to its high conversion.

Acknowledgments

Thanks are due to Andrea Ardu and to the 'Centro Servizi di Ateneo per la Ricerca (CeSAR)' for the use of the TEM/EDX measurements performed with JEOL JEM 1400-PLUS. The catalytic tests have been performed by SOTACARBO within the Advanced Sustainable technologieS for Energy Transition, ASSET project (CUP D43C22002400002), funded by the Regional Government of Sardinia.

Author Contributions

Conceptualization: [Francesca Ferrara and Elisabetta Rombi]; Data curation: [Luciano Atzori, Sarah Lai, Maria Giorgia Cutrufello, and Mauro Mureddu]; Formal analysis: [Luciano Atzori, Sarah Lai, Francesca Ferrara, Mauro Mureddu, and Elisabetta Rombi]; Funding acquisition: [Alberto Pettinau]; Investigation: [Luciano Atzori, Sarah Lai, Maria Giorgia Cutrufello, Mauro Mureddu, and Elisabetta Rombi]; Methodology: [Luciano Atzori, Mauro Mureddu, and Elisabetta Rombi]; Project administration: [Francesca Ferrara and Elisabetta Rombi]; Resources: [Maria Giorgia Cutrufello, Francesca Ferrara, Alberto Pettinau, and Elisabetta Rombi]; Supervision: [Francesca Ferrara, Alberto Pettinau, and Elisabetta Rombi]; Validation: [Luciano Atzori, Sarah Lai, Maria Giorgia Cutrufello, Francesca Ferrara, Mauro Mureddu,

and Elisabetta Rombi]; Visualization: [Luciano Atzori, Sarah Lai, Maria Giorgia Cutrufello, Mauro Mureddu, and Elisabetta Rombi]; Writing – original draft: [Luciano Atzori, Sarah Lai, Maria Giorgia Cutrufello, Mauro Mureddu, and Elisabetta Rombi]; Writing – review & editing: [Luciano Atzori, Sarah Lai, Maria Giorgia Cutrufello, Mauro Mureddu, and Elisabetta Rombi].

Declarations

Conflict of interest There are no known competing financial interests or personal relationships that could have appeared to influence the work reported in this paper.

References

1. T.A. Atsbha, T. Yoon, P. Seongho, C.-J. Lee, J. CO_2 Util. **44**, 101413 (2021)
2. A.A. Tountas, G.A. Ozin, M.M. Sain, Nat. Catal. **4**, 934–942 (2021)
3. G.A. Olah, Angew. Chem. Int. Ed. **52**, 104–107 (2013)
4. J. Sehested, J. Catal. **371**, 368–375 (2019)
5. I.U. Din, M.S. Shaharun, M.A. Alotaibi, A.I. Alharthi, A. Naeem, J. CO_2 Util. **34**, 20–33 (2019)
6. C. Li, X. Yuan, K. Fujimoto, Appl. Catal. A Gen. **469**, 306–311 (2014)
7. B. Liang, J. Ma, X. Su, C. Yang, H. Duan, H. Zhou, S. Deng, L. Li, Y. Huang, Ind. Eng. Chem. Res. **58**, 9030−9037 (2019)
8. J. Zhong, X. Yang, Z. Wu, B. Liang, Y. Huang, T. Zhang, Chem. Soc. Rev. **49**, 1385–1413 (2020)
9. F. Sha, Z. Han, S. Tang, J. Wang, C. Li, ChemSusChem **13**, 6160–6181 (2020)
10. X. Jiang, X. Nie, X. Guo, C. Song, J.G. Chen, Chem. Rev. **120**, 7984−8034 (2020)
11. M. Ren, Y. Zhang, X. Wang, H. Qiu, Catalysts **12**, 403 (2022)
12. K. Li, J.G. Chen, ACS Catal. **9**, 7840–7861 (2019)
13. X. Guo, D. Mao, G. Lu, S. Wang, G. Wu, J. Mol. Catal. A Chem. **345**, 60–68 (2011)
14. H. Ban, C. Li, K. Asami, K. Fujimoto, Catal. Commun. **54**, 50−54 (2014)
15. S. Li, Y. Wang, B. Yang, L. Guo, Appl. Catal. A Gen. **571**, 51−60 (2019)
16. T. Phongamwong, U. Chantaprasertporn, T. Witoon, T. Numpilai, Y. Pooarporn, W. Limphirat, W. Donphai, P. Dittanet, M. Chareonpanich, J. Limtrakul, Chem Eng. J. **316**, 692–703 (2017)
17. J. Słoczyński, R. Grabowski, A. Kozłowska, P. Olszewski, M. Lachowska, J. Skrzypek, J. Stoch, Appl. Catal. A Gen. **249**, 129–138 (2003)
18. H. Ren, C.-H. Xu, H.-Y. Zhao, Y.-X. Wang, J. Liu, J.-Y. Liu, J. Ind. Eng. Chem. **28**, 261–267 (2015)

19. X. Guo, D. Mao, S. Wang, G. Wu, G. Lu, Catal. Commun. **10**, 1661–1664 (2009)
20. X. Dong, F. Li, N. Zhao, F. Xiao, J. Wang, Y. Tan, Appl. Catal. B Environ. **191**, 8–17 (2016)
21. X. Guo, D. Mao, G. Lu, S. Wang, G. Wu, J. Catal. **271**, 178–185 (2010)
22. C. Paris, A. Karelovic, R. Manrique, S. Le Bras, F. Devred, V. Vykoukal, A. Styskalik, P. Eloy, D.P. Debecker, ChemSusChem **13**, 6409-6417 (2020)
23. J.Y. Liu, J.L. Shi, D.H. He, Q.J. Zhang, X.H. Wu, Y. Liang, Q.M. Zhu, Appl. Catal. A Gen. **218**, 113–119 (2001)
24. A. Karelovic, A. Bargibant, C. Fernández, P. Ruiz, Catal. Today **197**, 109–118 (2012)
25. G. Wang, Y. Zuo, M. Han, Appl. Catal. A Gen. **394**, 281–286 (2011)
26. K. Samson, M. Śliwa, R.P. Socha, K. Gora-Marek, D. Mucha, D. Rutkowska-Zbik, J-F. Paul, M. Ruggiero-Mikołajczyk, R. Grabowski, J. Słoczynski, ACS Catal. **4**, 3730−3741 (2014)
27. Y. Cui, X. Lian, L. Xu, M. Chen, B. Yang, C.-e. Wu, W. Li, B. Huang, X. Hu, Materials **12**, 276 (2019)
28. D. Gu, F. Schüth, Chem. Soc. Rev. **43**, 313–344 (2014)
29. L. Qi, Q. Yu, Y. Dai, C. J. Tang, L. J. Liu, H. L. Zhang, F. Gao, L. Dong, Y. Chen, Appl. Catal. B Environ. **119-120**, 308-320 (2012)
30. B. Sun, X.L. Xu, G.W. Zhou, Adv. Mater. Res. 918, 12–16 (2014)
31. C. Hu, X. Zhang, W. Li, Y. Yan, G. Xi, H. Yang, J. Li, H. Bai, J. Mater. Chem. A **2**, 2040–2043 (2014)
32. H. Liu, T. Liu, X. Dong, Z. Zhu, Mater. Lett. **134**, 240–243 (2014)
33. L. Li, D. Mao, J. Yu, X. Guo, J. Power Sources **279**, 394–404 (2015)
34. F.C.F. Marcos, L. Lin, L.E. Betancourt, S.D. Senanayake, J.A. Rodriguez, J.M. Assaf, R. Giudici, E.M. Assaf, J. CO_2 Util. **41**, 101215 (2020)
35. Y. Wang, J. Ma, M. Luo, P. Fang, M. He, J. Rare Earths **25**, 58–62 (2007)
36. M.F Luo, J.M. Ma, J.Q. Lu, Y.P. Song, Y.J. Wang, J. Catal. **246**, 52-59 (2007)
37. H.P. Klug, L.E. Alexander. X-ray Diffraction Procedures: For Polycrystalline and Amorphous Materials, 2nd edn. (Wiley & Sons Inc., New York, 1974) pp. 687–703
38. F. Rouquerol, J. Rouquerol, K.S.W. Sing, P. Llewellyn, G. Maurin, Adsorption by Powders and Porous Solids: Principles, Methodology and Applications, 2nd edn. (Academic Press-Elsevier, Amsterdam, 2014), pp. 12-13.
39. A. Gervasini, S. Bennici, Appl. Catal. A Gen. **281**, 199–205 (2005)
40. K.D. Jung, O.S. Joo, S.H. Han, Catal. Lett. **68**, 49–54 (2000)
41. A.L. Borer, R. Prins, J. Catal. 144, 439–445 (1993)
42. K. Taira, R. Murao, Energies **14**, 7922 (2021)

43. L. Atzori, E. Rombi, D. Meloni, R. Monaci, M.F. Sini, M.G. Cutrufello, J. Nanosci. Nanotechnol. **19**, 3269–3276 (2019)
44. J. Yang, K. Hidajat, S. Kawi, J. Mater. Chem. **19**, 292-298 (2009)
45. L. Atzori, M.G. Cutrufello, D. Meloni, C. Cannas, D. Gazzoli, R. Monaci, M.F. Sini, E. Rombi, Catal. Today **299**, 183–192 (2018)
46. T. Witoon, T. Permsirivanich, W. Donphai, A. Jaree, M. Chareonpanich, Fuel Process. Technol. **116**, 72–78 (2013)
47. J. Słoczyński, R. Grabowski, A. Kozłowska, P.K. Olszewski, J. Stoch, Phys. Chem. Chem. Phys. **5**, 4631–4640 (2003)
48. D.M. Ruthven, Principles of adsorption & adsorption processes (Wiley, New York, 1984)
49. T. Witoon, N. Kachaban, W. Donphai, P. Kidkhunthod, K. Faungnawakij, M. Chareonpanich, J. Limtrakul, Energy Convers. Manag. **118**, 21–31 (2016)
50. M. Mureddu, F. Ferrara, A. Pettinau, Appl. Catal. B Environ. **258**, 117941 (2019)
51. S.F.H. Tasfy, N.A.M. Zabidi, M.S. Shaharun, Int. J. Chem., Mol., Nuclear, Mater. Metall. Eng. **11**, 108–113 (2017)
52. M. Mureddu, S. Lai, L. Atzori, E. Rombi, F. Ferrara, A. Pettinau, M.G. Cutrufello, Catalysts **11**, 615 (2021)
53. G. Bonura, F. Arena, G. Mezzatesta, C. Canilla, L. Spadaro, F. Frusteri, Catal. Today **171**, 251–256 (2011)
54. L. Angelo, K. Kobl, L.M. Martinez Tejada, Y. Zimmermann, K. Parkhomenko, C. R. Chim. **18**, 250–260 (2015)
55. C. Zhong, X. Guo, D. Mao, S. Wang, G. Wu, G. Lu, RSC Adv. **5**, 52958 (2015)
56. N.D. Nielsen, J. Thrane, A.D. Jensen, J.M. Christensen, Catal. Lett. **150**, 1427–1433 (2020).
57. G. Bonura, M. Cordaro, C. Cannilla, F. Arena, F. Frusteri, Appl. Catal. B Environ. **152-153**, 152-161 (2014)
58. P. Gao, F. Li, H. Zhan, N. Zhao, F. Xiao, W. Wei, L. Zhong, H. Wang, Y. Sun, J. Catal. **298**, 51–60 (2013)
59. X. Guo, D. Mao, G. Lu, S. Wang, G. Wu, Catal. Commun. **12**, 1095–1098 (2011)
60. J. Skrzypek, J. Słoczyński, S. Ledakowicz, Methanol Synthesis (Polish Scientific Publishers (PWN), Warszawa, 1994) p. 54.
61. P. Gao, F. Li, F.K. Xiao, N. Zhao, N.N. Sun, W. Wei, L.S. Zhong, Y.H. Sun, Catal. Sci. Technol. **2**, 1447−1454 (2012)
62. P. Gao, F. Li, H.J. Zhan, N. Zhao, F.K. Xiao, W. Wei, L.S. Zhong, H. Wang, Y.H. Sun, J. Catal. **298**, 51−60 (2013)
63. X.S. Dong, F. Li, N. Zhao, F.K. Xiao, J.W. Wang, Y.S. Tan, Appl. Catal. B Environ. **191**, 8−17 (2016)
64. F.C.F. Marcos, L. Lin, L.E. Betancourt, S.D. Senanayake, J.A. Rodriguez, J.M. Assaf, R. Giudici, E.M. Assaf, J. CO_2 Util. **41**, 101215 (2020)
65. H.J. Zhan, F. Li, P. Gao, N. Zhao, F.K. Xiao, W. Wei, L.S. Zhong, Y.H. Sun, J. Power Sources **251**, 113−121 (2014)
66. O. Tursunov, L. Kustov, Z. Tilyabaev, J. Taiwan Inst. Chem. Eng. **78**, 416-422 (2017)

67. H. Ren, C.H. Xu, H.Y. Zhao, Y.X. Wang, J. Liu, J. Ind. Eng. Chem. **28**, 261–267 (2015)

68. W. Cai, P.R. de la Piscina, J. Toyir, N. Homs, Catal. Today **242**, 193–199 (2015)